DE GRUYTER DOI 10.1515/zkri-2013-1626 — Z. Kristallogr. 2014; 229(2): 63–76

Paolo Lotti, G. Diego Gatta*, Nicola Rotiroti, Fernando Cámara and George E. Harlow

The high-pressure behavior of balliranoite: a cancrinite-group mineral

Abstract: The high-pressure elastic behavior and structure evolution of a natural balliranoite, *i.e.* a mineral isotypic with cancrinite belonging to the davyne subgroup, $(Na_{4.47}Ca_{2.86}K_{0.11})(Si_{5.96}Al_{6.04}O_{24})Cl_{2.03}(CO_3)_{0.78}(SO_4)_{0.33}$, $a = 12.680(1)$ Å, $c = 5.3141(5)$ Å and $V = 739.9(1)$ Å^3, S.G. $P6_3$, have been studied by means of *in-situ* single-crystal X-ray diffraction with a diamond anvil cell, up to 6.77(2) GPa. No evidence of phase transition, structure collapse or change of the compressional behavior have been observed within the pressure range investigated. The unit-cell volume evolution as function of pressure has been fitted with a second-order Birch-Murnaghan equation of state (BM EoS), yielding the following refined parameters: $V_0 = 735.5(7)$ Å^3, $K_{V0} = 48.1(8)$ GPa. Fitting of the a vs. P and c vs. P data with linearized third-order BM-EoS leads to the following elastic anisotropy at ambient conditions: $K_{a0} : K_{c0} = 1.35 : 1$. The P-induced structure evolution of balliranoite is mainly governed by the framework re-arrangement through tilting of quasi-rigid tetrahedra. A comparative analysis of the elastic behavior and of the structure deformation mechanisms of balliranoite and cancrinite at high-pressure are carried out.

Keywords: high pressure, balliranoite, cancrinite, davyne, equation of state

*Corresponding Author: Diego Gatta, Dipartimento di Scienze della Terra, Università degli Studi di Milano, via Botticelli 23, 20133 Milano, Italy, e-mail: diego.gatta@unimi.it
Paolo Lotti, Nicola Rotiroti: Dipartimento di Scienze della Terra, Università degli Studi di Milano, via Botticelli 23, 20133 Milano, Italy
Fernando Cámara: Dipartimento di Scienze della Terra, Università degli Studi di Torino, via Valperga Caluso 35, 10125 Torino, Italy
George E. Harlow: Department of Earth and Planetary Sciences, American Museum of Natural History, New York, NY 10024-5192, U.S.A.

1 Introduction

Balliranoite is a rare member of the cancrinite group, which consists of eleven natural species and several synthetic compounds (Bonaccorsi and Merlino 2005; Pekov et al. 2011 and references therein), all sharing the [CAN]-topology of the tetrahedral framework (Baerlocher et al. 2007) (Figs. 1–3). These isotypic materials belong to the ABC-6 framework-family, with structures built by layers made by single six-membered rings of tetrahedra (non-interconnected within the layers) in A, B or C positions. Different stacking sequences give rise to various tetrahedral topologies: the simplest ABAB sequence results in the [CAN]-framework type. In the [CAN]-framework each single six-membered ring within the layers is perpendicular to the [0001] crystallographic direction (hereafter S6R ⊥ [0001]) and is bound to three rings in the previous layer and three rings in the next one (Fig. 1). The resulting structure is made by columns of base-sharing *can* units (or cancrinite cages, undecahedral cages, $4^6 6^5$ units) (McCusker et al. 2001), where the bases correspond to the S6R ⊥ [0001] (Figs. 1, 2). These columns surround iso-oriented channels, parallel to [0001] and bound by twelve-membered rings of tetrahedra (12R), with a free diameter of 5.9 Å (Baerlocher et al. 2007) (Figs. 1–3). Double *zigzag* chains of tetrahedra (*dzc* units), made by edge-sharing four-membered rings (S4R), run along the *c*-axis bordering single six-membered rings windows, approximately parallel to [0001] (hereafter S6R ∠ [0001]), which act as joint unit between cages and channels (Figs. 1, 2).

All the cancrinite-group minerals, except cancrisilite and tiptopite (Bonaccorsi and Merlino 2005), display a perfectly ordered aluminosilicate framework with compo-

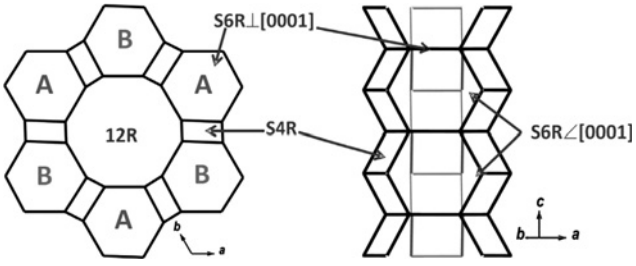

Fig. 1: (*Left*). A "skeletal" view of the [CAN] framework down [0001]. The A and B positions of the S6R⊥ [0001] are shown. (*Right*). A "skeletal" representation of a column of base-sharing *can* units with a perspective view of the double *zigzag* chains, made by S4R of tetrahedra, running along [0001].

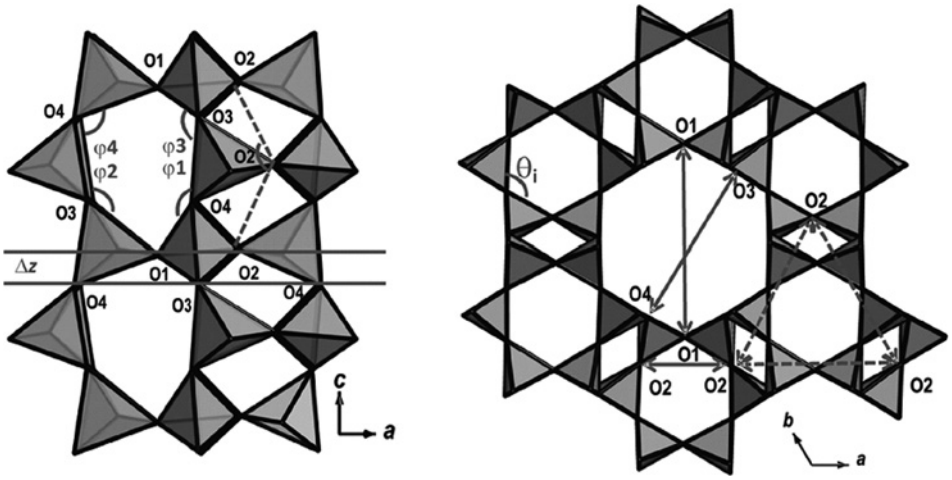

Fig. 2: A column of *can* units (on the left) and the [CAN] framework viewed down [0001] (on the right). Relevant distances and angles are shown. Three symmetry-related $(O2–O2)_{cw}$ distances ("cage width") are drawn as dashed lines. The $(O2–O2)_R$ distance is drawn as a solid line.

sition ($Al_6Si_6O_{24}$). Two subgroups can be defined according to the nature of the extraframework population filling the columns of *can* units: a) the cancrinite subgroup, where alternated Na–H_2O clusters give rise to chains of non-equally spaced Na–$H_2O\cdots$Na–H_2O and b) the davyne subgroup, where chains of almost equally spaced Ca–Cl–Ca–Cl occur (Fig. 4). Channels are occupied by alkaline and earth-alkaline cations (Na^+, K^+, Ca^{2+}) close to the walls and various anionic and/or molecular groups near the center (Fig. 4). Among them, the most common in natural species are CO_3^{2-}, SO_4^{2-} and Cl^-. Within the davyne subgroup, the occurrence of SO_4^{2-} and Cl^- induces geometrical constraints on the configuration of the channel population, which can result in an ordering within and between adjacent channels, as occurs in the (SO_4^{2-})- and (Cl^-)-end members microsommite (Bonaccorsi et al. 2001) and quadridavyne (Bonaccorsi et al. 1994), respectively, both showing a superstructure within the (0001) plane (further details are in Bonaccorsi and Merlino 2005). A long-range disorder of the channel population is found in davyne (Bonaccorsi et al. 1990; Hassan and Grundy 1990; Bonaccorsi et al. 1995; Rozenberg et al. 2009), which can be considered as an intermediate member between microsommite and quadridavyne (Bonaccorsi and Merlino 2005). The first evidence of davyne samples having CO_3^{2-} as the dominant anionic species (i.e. the analogue of cancrinite) was reported by Ballirano et al. (1996, 1998) and later by Binon et al. (2004) before the (CO_3^{2-})-davyne was recognized as a new mineral species by the IMA Commission on New Minerals, Nomenclature and Classification, with the name *balliranoite*. Crystal structure, chemical and optical properties of holotype balliranoite have been reported by Chukanov et al. (2010). Despite the paucity of references in the literature,

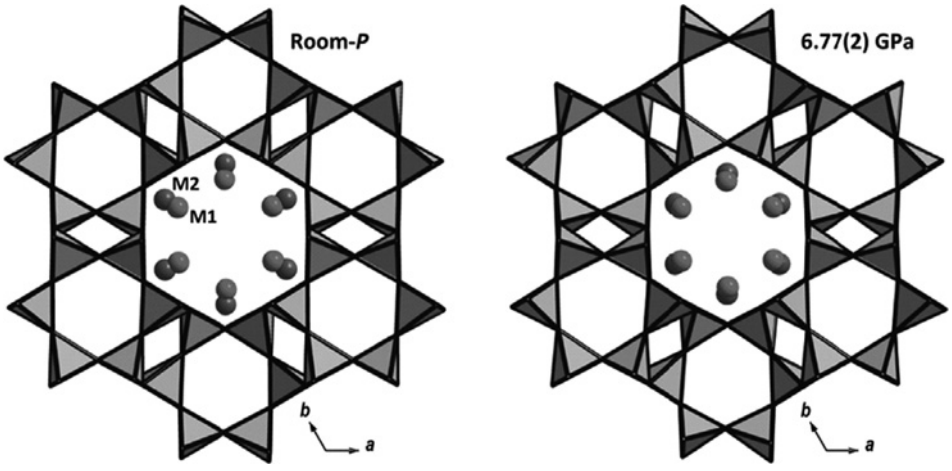

Fig. 3: The [CAN] framework and the channel cations viewed down [0001] at room conditions and 6.77(2) GPa, respectively.

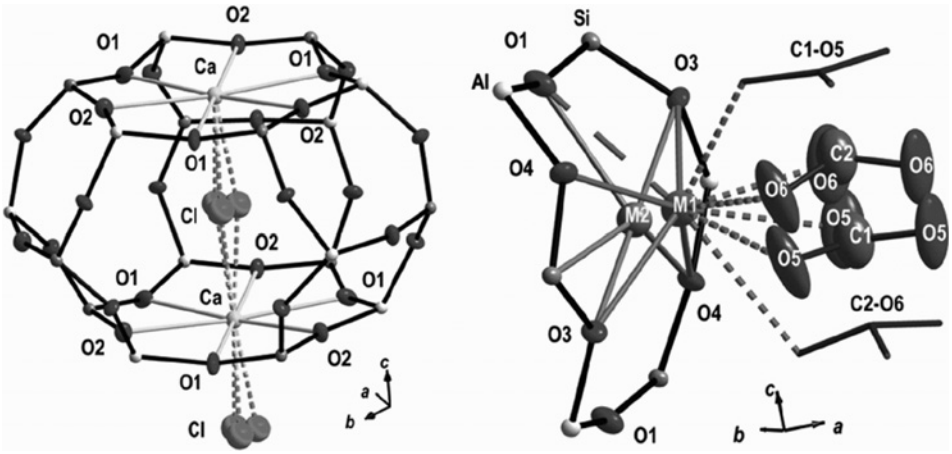

Fig. 4: (*Left*). The extraframework population of the *can* unit with a view of the Ca coordination shell. Dashed lines represent mutually exclusive bonds between Ca and the Cl atoms lying out of the 3-fold axis. (*Right*). Coordination shells of the M1 and M2 channel cations. Dashed lines represent statistical bonds between M1 and carbonate oxygen atoms. At low pressure, O1 is likely too far for an effective bond with a Na atom in M1 (see Section 5.2. for further details).

in consideration of the problematic characterization and classification of davyne subgroup minerals in the past, as thoroughly reported by Bonaccorsi et al. (1990), a more common occurrence of this mineralogical species cannot be excluded.

Natural occurrences of cancrinite-group minerals are in alkali-rich and silica-undersaturated environments (Deer et al. 2004; Bonaccorsi and Merlino 2005). They can mainly be found in nepheline syenite intrusions as late-stage hydrothermal crystallizations or as replacement products of nepheline and sodalite, and in related volcanic rocks. They are also common phases in metamorphic environments related to alkali-rich magmatic intrusions in carbonate wall rocks (i.e. skarns). According to Pekov et al. (2010), cancrinite subgroup members are common in intrusive alkaline rocks, where they crystallize during the post-magmatic stages, whereas the other cancrinite-group minerals (including davyne-subgroup) are most commonly found in effusive and metamorphic environments.

Several synthetic "cancrinites" with highly variable framework and extraframework crystal chemistries have been obtained so far (Bonaccorsi and Merlino 2005; Sirbescu and Jenkins 1999 and references therein). Although stacking faults (insertion of hexagonal layers in a C position) and the concomitant presence of cationic and anionic species within the channel result in a reduced ionic exchange capacity, complete Na ↔ Li and Na ↔ Ag exchanges have been reported for synthetic hydroxy-cancrinite (Barrer and Falconer 1956). Partial substitutions of channel-Na with K and Tl have also been reported for a Na-rich davyne (Bonaccorsi and Merlino 2005). In addition, cancrinite-group minerals are involved in several non-natural processes of environmental and economic interest, a short summary of which is reported by Gatta et al. (2013).

Due to the large crystal-chemical variability shown by both natural and synthetic cancrinite-group minerals (Bonaccorsi and Merlino 2005), a systematic investigation among the end-members is necessary, in order to explore the potential role played by the different extraframework population on the thermo-elastic behavior of these minerals. Although a few studies on the high-temperature behavior of [CAN]-framework compounds have been reported (e.g. Hassan et al. 2006; Hassan 1996; Fechtelkord *et al.* 2001; Bonaccorsi et al. 1995, 2001, 2007), very little can be found about high-pressure (e.g. Gatta and Lee 2008; Oh *et al.* 2011) or low-temperature conditions. The present work is part of a larger study aimed to provide a model of the thermo-elastic behavior and structure evolution of the cancrinite-group minerals at non-ambient conditions. So far, the low-temperature (Gatta et al. 2012) and high-pressure (Lotti et al. 2012) behavior of cancrinite and the low-temperature behavior of balliranoite (Gatta et al. 2013) have been described. The high-pressure behavior of balliranoite, by *in-situ* single-crystal X-ray diffraction, is here reported along with a comparison with the *P*-induced cancrinite evolution.

2 Materials and experimental methods

The natural sample of balliranoite used in this study is from Dattaw, Mogok metamorphic belt, Myanmar (#108339, collection of the American Museum of Natural

Table 1: Details pertaining to the intensity data collections, unit-cell parameters and structure refinements of balliranoite at different pressures.

P (GPa)	0.0001 (P_{0-AIR})	0.0001 (P_{0-DAC})	0.85(3) (P_1)	1.73(3) (P_2)	2.62(4) (P_3)	3.80(5) (P_4)	4.95(3) (P_5)	5.95(4) (P_6)	6.77(2) (P_7)
Scan width (°/frame)	1	0.5	0.5	0.5	0.5	0.5	0.5	0.5	0.5
a (Å)	12.680(1)	12.669(3)	12.594(5)	12.558(3)	12.502(3)	12.426(3)	12.360(4)	12.289(4)	12.277(3)
c (Å)	5.3141(5)	5.3171(9)	5.284(1)	5.2518(8)	5.2199(9)	5.1780(8)	5.1348(9)	5.100(1)	5.095(1)
V (Å^3)	739.9(1)	739.1(4)	725.6(6)	717.3(4)	706.6(4)	692.4(4)	679.4(5)	667.1(5)	665.1(4)
Maximum 2θ (°)	72.61	61.01	60.64	60.98	60.97	61.01	60.95	60.75	60.82
Measured reflections	19175	3350	3300	3323	3378	3147	3183	3105	3072
Unique reflections	2085	973	964	974	952	930	903	894	884
Unique reflections with $F_o > 4\sigma(F_o)$	1405	444	459	495	516	488	488	460	414
R_{int}	0.0621	0.0859	0.0811	0.0874	0.0766	0.0858	0.1007	0.1241	0.0963
Number of l.s. parameters	103	43	43	43	43	43	43	43	43
R_1, $F_o > 4\sigma(F_o)$	0.0447	0.0517	0.0574	0.0556	0.0536	0.0571	0.0621	0.0729	0.0600
R_1, all data	0.0947	0.1236	0.1217	0.1141	0.1024	0.1110	0.1196	0.1411	0.1333
wR^2	0.0450	0.0682	0.0705	0.0724	0.0724	0.0698	0.0772	0.0971	0.0785
GooF	1.017	1.026	1.036	1.017	1.073	1.010	1.073	1.220	1.035
Residuals (e$^-$/ Å^3)	+0.83/ −0.67	+0.93/ −0.90	+0.71/ −0.71	+0.58/ −0.61	+0.67/ −0.71	+0.63/ −0.77	+1.06/ −0.77	+1.18/ −1.04	+0.93/ −0.91

Scan type: ω/φ; Exposure time: 60 s/frame; Space group: $P6_3$; $Z = 1$
$R_{int} = \sum |F^2_{obs} - (\text{mean})| / \sum [F^2_{obs}]$; $R_1 = \sum ||F_{obs}| - |F_{calc}|| / \sum |F_{obs}|$; $wR_2 = \{\sum [w(F^2_{obs} - F^2_{calc})^2] / \sum [w(F^2_{obs})^2]\}^{0.5}$, $w = 1/[\sigma^2(F^2_{obs}) + (0.01 \cdot P)^2]$, $P = [\text{Max}(F^2_{obs}, 0) + 2 \cdot F^2_{calc}]/3$.

History, New York, USA), in an assemblage of corundum (ruby), marialite (mizzonite) and, presumably calcite (sample was trimmed before acquisition). Balliranoite likely crystallized in a skarn-like environment by the interaction of granite and its fluids with the marble wall-rocks and corundum inclusions (Harlow and Bender 2013, and references therein). The same sample of balliranoite was used by Gatta et al. (2013) for low-T experiments. A single-crystal ($160 \times 100 \times 70$ μm^3), optically free of defects, was selected for the high-pressure diffraction experiments of this study. The crystal-chemical formula, from electron microprobe analysis in wavelength-dispersive mode, is $(Na_{4.47}Ca_{2.86}K_{0.11})(Si_{5.96}Al_{6.04}O_{24})Cl_{2.03}(CO_3)_{0.78}(SO_4)_{0.33}$. Further details about the chemical analysis protocol are in Gatta et al. (2013).

An X-ray diffraction intensity data collection was first performed with the crystal in air using an Oxford Diffraction Xcalibur diffractometer, operating at 50 kV and 40 mA, with a monochromatized Mo$K\alpha$ radiation and equipped with a CCD detector at 80 mm from the sample position. A combination of ω/φ scans, with step scan 1° and exposure time 60 s per frame, was used to maximize redundancy and data coverage. A total of 19175 measured reflections showed a metrically hexagonal lattice with: $a = 12.680(1)$ Å, $c = 5.3141(5)$ Å and $V = 739.9(1)$ Å^3 (Table 1). Systematic absences were compatible with the $P6_3$ space group and no superstructure reflections were observed. Intensity data were then integrated and corrected for Lorentz-polarization (Lp) effects using the Crysalis software (Agilent 2012). Absorption due to the crystal was found to be not significant.

In-situ HP-experiments were performed with an ETH-type diamond anvil cell (DAC) with Be backing plates (Miletich et al. 2000). A T301 steel foil was used as a gasket, with a micro-hole (diameter ~300 μm) drilled by spark-erosion as P-chamber, after the gasket was pre-indented to a thickness of about 120 μm. A nominally anhydrous mixture (methanol : ethanol = 4 : 1) was used as hydrostatic P-transmitting medium (Angel et al. 2007), whereas a standard crystal of quartz, loaded along with the balliranoite sample in the P-chamber, was used as pressure calibrant (Angel et al. 1997). The balliranoite unit-cell parameters were measured from 0.0001 (crystal in the DAC without P-medium) to 6.77(2) GPa (Table 2), by centering a list of 32 Bragg reflections with a KUMA-KM4 point-detector diffractometer. Operating conditions were 50 kV and 40 mA with a monochromatized Mo$K\alpha$ radiation. X-ray intensity data were collected at 0.0001, 0.85(3), 1.73(3), 2.62(4), 3.80(5), 4.95(3), 5.95(4) and 6.77(2) GPa using the Oxford Diffraction Xcalibur CCD-diffractometer at the same operating conditions used for the crystal in air. A combination of ω/φ scans was used for all the high pressure data collections, with step scan 0.5° and exposure time 60 s per frame. Reflections conditions compatible with $P6_3$ space group are always observed within the P-range investigated. Intensity data

Table 2: Unit-cell parameters at different pressures measured using a KUMA KM4 point-detector diffractometer.

P (GPa)	*a* (Å)	*c* (Å)	*V* (Å^3)
0.0001*	12.652(9)	5.304(3)	735(1)
0.14(2)	12.640(7)	5.298(3)	733(1)
0.85(3)	12.594(9)	5.268(3)	724(1)
1.21(2)	12.566(10)	5.255(4)	719(2)
1.41(3)	12.549(11)	5.248(4)	716(2)
1.73(3)	12.530(10)	5.233(3)	712(2)
2.00(4)	12.508(9)	5.223(2)	708(1)
2.36(4)	12.486(10)	5.210(3)	703(2)
2.62(4)	12.471(9)	5.199(2)	700(1)
3.12(3)	12.436(11)	5.183(3)	694(2)
3.24(4)	12.431(10)	5.179(3)	693(2)
3.80(5)	12.396(10)	5.160(3)	687(2)
4.14(5)	12.374(12)	5.146(3)	682(2)
4.60(5)	12.351(12)	5.131(3)	678(2)
4.95(3)	12.324(11)	5.120(3)	673(2)
5.40(4)	12.304(9)	5.108(2)	670(1)
5.74(6)	12.290(10)	5.097(3)	667(1)
5.95(4)	12.279(11)	5.090(3)	665(2)
6.22(3)	12.265(10)	5.085(3)	662(1)
6.57(2)	12.252(9)	5.075(2)	660(1)
6.77(2)	12.241(10)	5.070(3)	658(1)

∗ With the crystal in the DAC without *P*-medium.

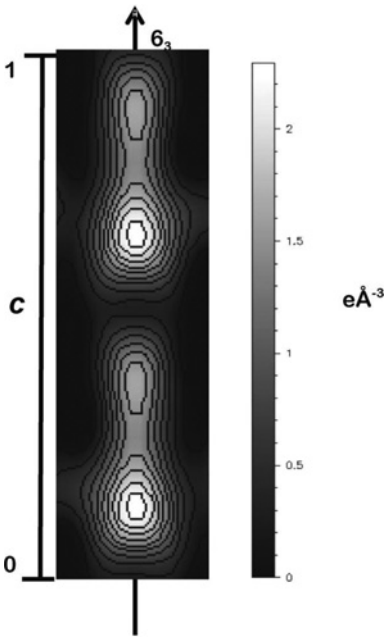

Fig. 5: Difference-Fourier map, phased without the CO_3^{2-} groups, showing the positional disorder along the 6_3 axis at the center of the 12R-channel.

were integrated and corrected for Lp-effects with the Crysalis software (Agilent 2012) and for absorption effects, due to the DAC, with the ABSORB software (Angel 2004). Further details pertaining to the data collections are in Table 1.

3 Structure refinement protocol

All the structure refinements were performed using the *SHELXL-97* software (Sheldrick 2008), integrated in the *WinGX* suite of crystallographic programs (Farrugia 1999). The neutral atomic scattering factors of O, Si, Al, Na, Ca, Cl and C were taken from the *International Tables of Crystallography Vol. C* (Wilson and Prince 1999). The balliranoite structure refinement was first performed from the data collected with the crystal in air. First cycles were carried out starting from the framework coordinates reported by Chukanov et al. (2010). The extraframework population was localized from the difference-Fourier synthesis of the electron density. The *can* units are filled by a Ca site (Ca), at the center of the S6R ⊥ [0001] on the 3-fold axis, and a Cl site (Cl), out of the 3-fold axis in three mutually exclusive positions (Fig. 4). The channel population is given by two mutually exclusive cation sites (M1 and M2) near the channel walls, as also reported by Chukanov et al. (2010) and Gatta et al. (2013), and two mutually exclusive configurations for the CO_3^{2-} groups (C1–O5 and C2–O6), with carbon atoms lying on the 6_3 axis at the channel center (Fig. 4). The difference-Fourier synthesis, calculated without the anionic groups, showed a highly disordered distribution of the electron density along the 6_3 axis (Fig. 5). This disorder hindered an unambiguous allocation of the SO_4^{2-} group, expected from the chemical analysis, as already reported by Gatta et al. (2013) even from X-ray single-crystal diffraction data collected at 108 K. The configuration of the sulphate group in the holotype mineral (Chukanov et al. 2010) was used, but unsuccessfully, suggesting that this configuration is not applicable to the balliranoite of this study. The M1 and M2 site occupancy factors (*sof*'s) were refined using the Na scattering factor, since a mixed Na/Ca curve did not improve the refinement figure of merit. No restriction was applied to *sof*'s of the carbonate groups (C1–O5 and C2–O6, respectively), in order to refine any potential contribution from the sulphate group. The Ca and Cl sites were set to a full occupancy (1.0 and 1/3, respectively, since only one of the three Cl sites out of the 3-axis can be simultaneously occupied). The first cycles were conducted with isotropic displacement parameters (*dp*'s), which were subsequently set to anisotropic, except for the M2 site because of significant correlation between the refined parameters. The C1–C2 and O5–O6 displacement parameters, respectively, were constrained to be equal in order to improve the refinement

Table 3: Atomic fractional coordinates, site occupancy factors (*sof*'s) and isotropic/equivalent displacement parameters (Å^2) at different pressures.

Site occupancy factors at P_0-AIR

Site	Occ.	Site	Occ.	Site	Occ.
Si	1.0	O4	1.0	C1	0.56(1)
Al	1.0	Ca	1.0	O5	0.575(8)
O1	1.0	Cl	$^1/_3$	C2	0.22(1)
O2	1.0	M1	0.881(6)	O6	0.165(9)
O3	1.0	M2	0.160(6)		

Site fractional coordinates

P (GPa)	Site	x	y	z	U_{iso}/U_{eq}
0.0001	Si	0.32757(5)	0.40840(5)	0.7568(1)	0.0088(1)
($P_{0\text{-AIR}}$)	Al	0.06970(5)	0.40846(5)	0.7581(1)	0.0092(1)
	O1	0.2127(1)	0.4268(1)	0.7068(3)	0.0187(4)
	O2	0.0998(1)	0.5565(1)	0.7465(4)	0.0169(3)
	O3	0.0101(1)	0.3312(2)	0.0387(3)	0.0147(5)
	O4	0.3131(2)	0.3407(2)	0.0214(3)	0.0163(4)
	Ca	$^1/_3$	$^2/_3$	0.7074(1)	0.0156(2)
	Cl	0.323(2)	0.683(2)	0.2115(3)	0.051(2)
	M1	0.1226(1)	0.2514(2)	0.2987(2)	0.0291(6)
	M2	0.1583(7)	0.324(1)	0.281(2)	0.031(2)
	C1	0	0	0.148(3)	0.054(4)
	C2	0	0	0.396(7)	0.054(4)
	O5	−0.0626(5)	0.0548(5)	0.147(2)	0.076(3)
	O6	−0.062(2)	0.052(2)	0.339(6)	0.076(3)
0.0001	Si	0.3278(2)	0.4085(2)	0.7553(4)	0.0100(3)
($P_{0\text{-DAC}}$)	Al	0.0698(2)	0.4091(2)	0.7566(5)	0.0100(3)
	O1	0.2145(4)	0.4284(4)	0.7025(7)	0.0170(6)
	O2	0.1010(3)	0.5575(4)	0.7477(9)	0.0170(6)
	O3	0.0120(5)	0.3316(5)	0.0371(6)	0.0170(6)
	O4	0.3140(6)	0.3415(5)	0.0221(7)	0.0170(6)
	Ca	$^1/_3$	$^2/_3$	0.7067(3)	0.0160(7)
	Cl	0.322(1)	0.686(1)	0.2127(6)	0.029(2)
	M1	0.1216(3)	0.2499(3)	0.3022(5)	0.029(1)
	M2	0.158(2)	0.318(19)	0.267(4)	0.029(1)
	C1	0	0	0.170(6)	0.080(5)
	C2	0	0	0.42(1)	0.080(5)
	O5	−0.0625(8)	0.0557(8)	0.166(2)	0.057(9)
	O6	−0.0625(8)	0.0557(8)	0.435(7)	0.057(9)
0.85(3)	Si	0.3275(2)	0.4084(2)	0.7588(4)	0.0104(3)
(P_1)	Al	0.0696(2)	0.4085(2)	0.7593(5)	0.0104(3)
	O1	0.2139(5)	0.4274(4)	0.6963(7)	0.0166(6)
	O2	0.1006(4)	0.5560(4)	0.7456(8)	0.0166(6)
	O3	0.0156(5)	0.3315(5)	0.0464(7)	0.0166(6)
	O4	0.3115(6)	0.3433(5)	0.0289(7)	0.0166(6)
	Ca	$^1/_3$	$^2/_3$	0.6994(3)	0.0175(7)
	Cl	0.319(1)	0.687(1)	0.2065(5)	0.020(1)
	M1	0.1218(4)	0.2494(4)	0.3083(5)	0.028(1)
	M2	0.157(2)	0.318(2)	0.274(4)	0.028(1)
	C1	0	0	0.161(5)	0.041(7)
	C2	0	0	0.410(8)	0.041(7)
	O5	−0.0619(9)	0.0563(9)	0.182(2)	0.068(4)
	O6	−0.0619(9)	0.0563(9)	0.445(6)	0.068(4)

Site fractional coordinates

P (GPa)	Site	x	y	z	U_{iso}/U_{eq}
1.73(3)	Si	0.3269(2)	0.4075(2)	0.7622(4)	0.0109(3)
(P_2)	Al	0.0689(2)	0.4078(2)	0.7630(5)	0.0109(3)
	O1	0.2121(5)	0.4255(4)	0.6898(7)	0.0168(6)
	O2	0.1010(3)	0.5568(4)	0.7461(8)	0.0168(6)
	O3	0.0190(5)	0.3333(5)	0.0554(7)	0.0168(6)
	O4	0.3090(5)	0.3446(5)	0.0379(7)	0.0168(6)
	Ca	$^1/_3$	$^2/_3$	0.6914(3)	0.0187(7)
	Cl	0.322(1)	0.6885(9)	0.1981(5)	0.023(1)
	M1	0.1216(3)	0.2490(3)	0.3167(5)	0.024(1)
	M2	0.152(2)	0.306(2)	0.286(3)	0.024(1)
	C1	0	0	0.159(5)	0.038(6)
	C2	0	0	0.399(8)	0.038(6)
	O5	−0.0612(9)	0.0564(9)	0.196(2)	0.069(4)
	O6	−0.0612(9)	0.0564(9)	0.444(6)	0.069(4)
2.62(4)	Si	0.3264(2)	0.4071(2)	0.7649(4)	0.0110(3)
(P_3)	Al	0.0688(2)	0.4072(2)	0.7661(5)	0.0110(3)
	O1	0.2103(5)	0.4243(4)	0.6857(7)	0.0171(6)
	O2	0.1005(4)	0.5577(4)	0.7452(8)	0.0171(6)
	O3	0.0203(5)	0.3334(5)	0.0615(7)	0.0171(6)
	O4	0.3071(6)	0.3449(5)	0.0455(7)	0.0171(6)
	Ca	$^1/_3$	$^2/_3$	0.6844(3)	0.0176(7)
	Cl	0.328(1)	0.6926(8)	0.1920(5)	0.022(1)
	M1	0.1217(3)	0.2489(3)	0.3237(5)	0.022(1)
	M2	0.148(2)	0.300(2)	0.286(4)	0.022(1)
	C1	0	0	0.158(5)	0.042(7)
	C2	0	0	0.396(8)	0.042(7)
	O5	−0.0621(9)	0.0557(9)	0.204(2)	0.061(3)
	O6	−0.0621(9)	0.0557(9)	0.439(6)	0.061(3)
3.80(5)	Si	0.3259(2)	0.4064(2)	0.7677(4)	0.0118(3)
(P_4)	Al	0.0693(2)	0.4070(2)	0.7693(5)	0.0118(3)
	O1	0.2092(5)	0.4222(4)	0.6813(7)	0.0169(5)
	O2	0.1010(4)	0.5578(4)	0.7428(7)	0.0169(5)
	O3	0.0244(4)	0.3357(5)	0.0693(7)	0.0169(5)
	O4	0.3050(5)	0.3476(5)	0.0536(7)	0.0169(5)
	Ca	$^1/_3$	$^2/_3$	0.6770(3)	0.0194(7)
	Cl	0.327(1)	0.6928(8)	0.1852(5)	0.022(1)
	M1	0.1214(4)	0.2487(3)	0.3307(5)	0.0209(9)
	M2	0.143(2)	0.291(2)	0.287(4)	0.0209(9)
	C1	0	0	0.170(5)	0.050(7)
	C2	0	0	0.443(8)	0.050(7)
	O5	−0.0624(8)	0.0566(8)	0.214(2)	0.051(3)
	O6	−0.0624(8)	0.0566(8)	0.404(6)	0.051(3)
4.95(3)	Si	0.3253(2)	0.4065(2)	0.7700(5)	0.0091(3)
(P_5)	Al	0.0691(2)	0.4068(2)	0.7726(6)	0.0091(3)
	O1	0.2086(5)	0.4208(5)	0.6775(8)	0.0137(6)
	O2	0.0991(4)	0.5561(4)	0.7422(8)	0.0137(6)
	O3	0.0256(5)	0.3353(5)	0.0751(8)	0.0137(6)
	O4	0.3030(6)	0.3484(6)	0.0587(8)	0.0137(6)
	Ca	$^1/_3$	$^2/_3$	0.6702(4)	0.0176(7)
	Cl	0.323(1)	0.691(1)	0.1789(6)	0.021(1)

Table 3: (Continued)

Site fractional coordinates					
P (GPa)	Site	*x*	*y*	*z*	U_{iso}/U_{eq}
	M1	0.1214(4)	0.2469(3)	0.3366(6)	0.019(1)
	M2	0.143(2)	0.289(2)	0.298(4)	0.019(1)
	C1	0	0	0.166(5)	0.049(8)
	C2	0	0	0.456(8)	0.049(8)
	O5	−0.0607(9)	0.0584(9)	0.222(2)	0.046(3)
	O6	−0.0607(9)	0.0584(9)	0.410(7)	0.046(3)
5.95(4)	Si	0.3253(2)	0.4061(2)	0.7722(7)	0.0105(4)
(P_6)	Al	0.0691(3)	0.4069(3)	0.7733(7)	0.0105(4)
	O1	0.2083(6)	0.4200(6)	0.675(1)	0.0121(7)
	O2	0.1001(5)	0.5575(5)	0.7402(9)	0.0121(7)
	O3	0.0282(6)	0.3375(6)	0.078(1)	0.0121(7)
	O4	0.3011(7)	0.3477(6)	0.063(1)	0.0121(7)
	Ca	$^1/_3$	$^2/_3$	0.6648(5)	0.0189(9)
	Cl	0.326(2)	0.694(1)	0.1753(8)	0.025(2)
	M1	0.1219(6)	0.2475(5)	0.3408(7)	0.020(1)
	M2	0.137(3)	0.278(3)	0.288(6)	0.020(1)
	C1	0	0	0.187(7)	0.05(1)
	C2	0	0	0.45(1)	0.05(1)
	O5	−0.062(1)	0.059(1)	0.224(2)	0.040(4)
	O6	−0.062(1)	0.059(1)	0.422(8)	0.040(4)
6.77(2)	Si	0.3253(2)	0.4062(2)	0.7730(6)	0.0110(3)
(P_7)	Al	0.0690(3)	0.4065(2)	0.7762(7)	0.0110(3)
	O1	0.2082(5)	0.4198(6)	0.6731(9)	0.0146(7)
	O2	0.1008(4)	0.5576(5)	0.7376(8)	0.0146(7)
	O3	0.0296(5)	0.3372(5)	0.0794(9)	0.0146(7)
	O4	0.3003(6)	0.3490(5)	0.0647(9)	0.0146(7)
	Ca	$^1/_3$	$^2/_3$	0.6620(5)	0.0222(8)
	Cl	0.319(1)	0.689(1)	0.1738(7)	0.024(2)
	M1	0.1208(5)	0.2463(4)	0.3425(6)	0.020(1)
	M2	0.139(2)	0.278(2)	0.288(6)	0.020(1)
	C1	0	0	0.189(6)	0.06(1)
	C2	0	0	0.46(1)	0.06(1)
	O5	−0.0625(9)	0.0583(9)	0.230(2)	0.046(4)
	O6	−0.0625(9)	0.0583(9)	0.423(8)	0.046(4)

stability. A racemic twinning with components ratio 0.53(4):0.47(4) was found. A test refinement excluded the possibility that the material had the corresponding centrosymmetric space group $P6_3/m$. Convergence was achieved leading to an R_1 factor of 0.0447 for 1405 reflections with $F_o > 4\sigma(F_o)$ and highest/lowest residual peaks in the difference-Fourier maps: +0.83 and −0.67 e/Å^3 (Table 1).

The high pressure structure refinements were performed starting from the model previously described. A set of restraints was applied in order to reduce the number of refined parameters, so as to compensate for the reduction in the number of observed reflections mainly due to the acces restrictions of the DAC. The site occupancy factors were all constrained to the values refined with the crystal in air and the atomic displacement parameters were all refined isotropic and constraining Si–Al, the framework oxygen sites, M1–M2, C1–C2 and O5–O6 to share the same values, respectively. Additionally, the C–O bond lengths were restrained to 1.300(5) Å and the carbonate oxygen sites (O5–O6) were constrained to share the same *x* and *y* coordinates, as they were found to be equal within 2σ from the refinement with the crystal in air. Convergence was always achieved with highest residual peaks in the difference-Fourier maps $\leq \pm 1.18$ e/Å^3. Further details pertaining to the structure refinements are in Table 1. Atomic coordinates, site occupancy factors and isotropic or equivalent displacement parameters are in Table 3. Anisotropic displacement parameters from the refinement at $P_{0\text{-AIR}}$ are deposited.

4 Results

4.1 Elastic behavior

The balliranoite of this study is stable up to the highest pressure here investigated, i.e. 6.77(2) GPa, with no evidence of phase transition or change of the compressional behavior. The unit-cell volume evolution as a function of *P* is shown in Fig. 6. The experimental data were fitted with a Birch-Murnaghan equation of state (Birch 1947; Angel 2000), truncated to the third order (III-BM EoS) and weighted for the experimental uncertainty in *P* and *V*, using the EoSFit v5.2 software (Angel 2000). The following parameters were determined: $V_0 = 735(1)$ Å^3, $K_{V0} = 48(3)$ GPa and $K_V' = 4.0(10)$. The refined K' value, supported by the horizontal trend of the normalized pressure as a function of the Eulerian strain ($F_e - f_e$ plot; Angel 2000) (Fig. 6), suggests that a truncation of the BM-EoS to the II-order, for which a $K' = 4$ is assumed (Angel 2000), is adequate to describe the elastic behavior of balliranoite. The fit to the experimental data of a II-BM EoS gives the following parameters: $V_0 = 735.5(7)$ Å^3, $K_{V0} = 48.1(8)$ GPa, which compare well with the weighted linear regression of the $F_e - f_e$ data, intercepting the F_e axis at 49(2) GPa (Fig. 6). The unit-cell edges evolution as a function of *P* is reported in Fig. 6: fitting the data with a "linearized" III-BM EoS (Angel 2000), weighted for the uncertainty in *P* and *l*, we obtained the following refined parameters: $a_0 = 12.654(6)$ Å, $K_{a0} = 54(4)$ GPa and $K_a' = 4.6(14)$; $c_0 = 5.305(2)$ Å, $K_{c0} = 40(2)$ GPa $K_c' = 3.3(6)$. The elastic anisotropy at ambient conditions can be represented by the ratio $K_{a0}:K_{c0} = 1.35:1$. The fit with a II-BM-EoS yielded the following parameters: $a_0 = 12.652(4)$ Å, $K_{a0} = 55(1)$ GPa; $c_0 = 5.306(2)$ Å, $K_{c0} = 37.6(5)$ GPa.

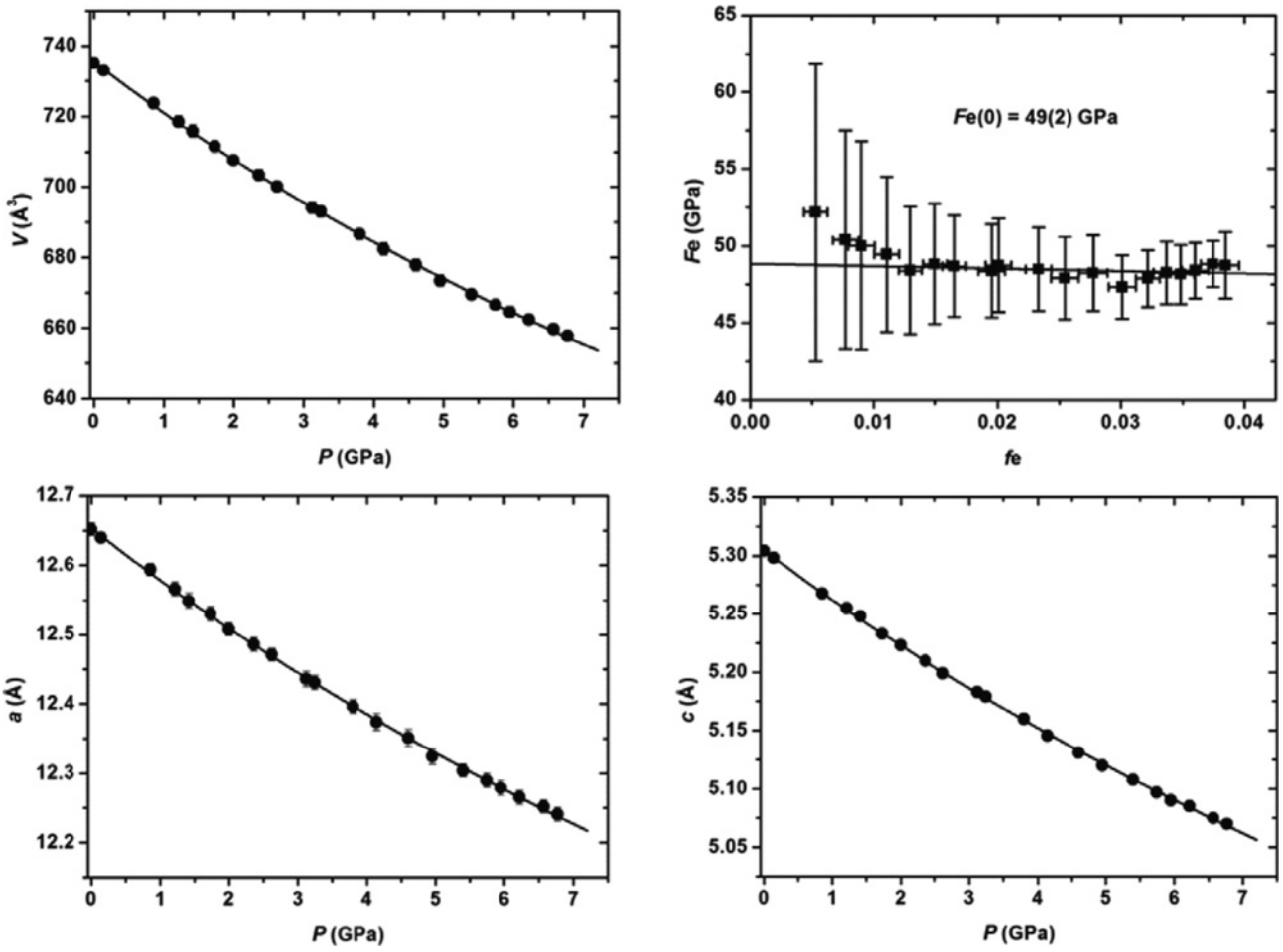

Fig. 6: (*Top*). On the left: unit-cell volume evolution as a function of pressure. The solid line represents the fit with a II-BM EoS. On the right: the normalized stress ($Fe = P/[3fe(1 + 2fe)^{5/2}]$) *vs*. the Eulerian finite strain ($fe = [(V_0/V)^{2/3} - 1]/2$) plot. The estimated standard deviations have been calculated according to Heinz and Jeanloz (1984). The solid line represents a weighted linear fit through the data. (*Bottom*). The *a* and *c* unit-cell parameters evolution as a function of pressure. The solid lines represent the fit with "linearized" III-BM EoS.

4.2 High-pressure structure evolution

The high-pressure structure evolution of this natural balliranoite can be described as mainly governed by the mutual tilting of the quasi-rigid framework tetrahedra. All of the Si–O–Al intertetrahedral angles decrease with pressure, though this deformation is significantly less intense for Si–O2–Al (Fig. 7; Table 4). The average ⟨Si–O⟩ and ⟨Al–O⟩ bond lengths at different pressures do not vary within the calculated standard deviations, even though a slight compression, especially for the AlO_4 tetrahedra, can be inferred (Table 4).

The pressure-induced tetrahedral tilting is reflected by several non-independent deformation mechanisms. Among those, within the (0001) plane can be represented by: 1) the ditrigonal rotation of the S6R ⊥ (0001) (described by the ditrigonal rotation angle, $\alpha = (\Sigma_i|120° - \theta_i|/2)/6$, where θ_i is the angle between the basal edges of neighboring tetrahedra articulated in the S6R, originally defined by Brigatti and Guggenheim, 2002, for the description of the structural evolution of phyllosilicates), which induces the shortening along the S6R ⊥ (0001) $(O2–O2)_R$ axis (Fig. 2; Table 4); 2) the *can* unit compression through the "cage width" $(O2–O2)_{cw}$ (dashed lines in Fig. 2) shortening (Fig. 7; Table 4); 3) the channel compression through the shortening of both the symmetrically independent diameters $(O3–O4)_{ch}$ and $(O1–O1)_{ch}$ (the latter being calculated as the projection onto the (0001) plane of the O1–O1 distance, as the involved O1 atoms are shifted along [0001] of $^1/_2 \cdot z$) (Figs. 2, 7; Table 4). Along the [0001] direction, the closure of the angles φ_1 (O1–O4–O3) and φ_2 (O1–O3–O4), coupled with the opening of φ_3 (O4–O3–O1) and φ_4 (O3–O4–O1) (Fig. 2; Table 4), reflects the compression of the double chain of tetrahe-

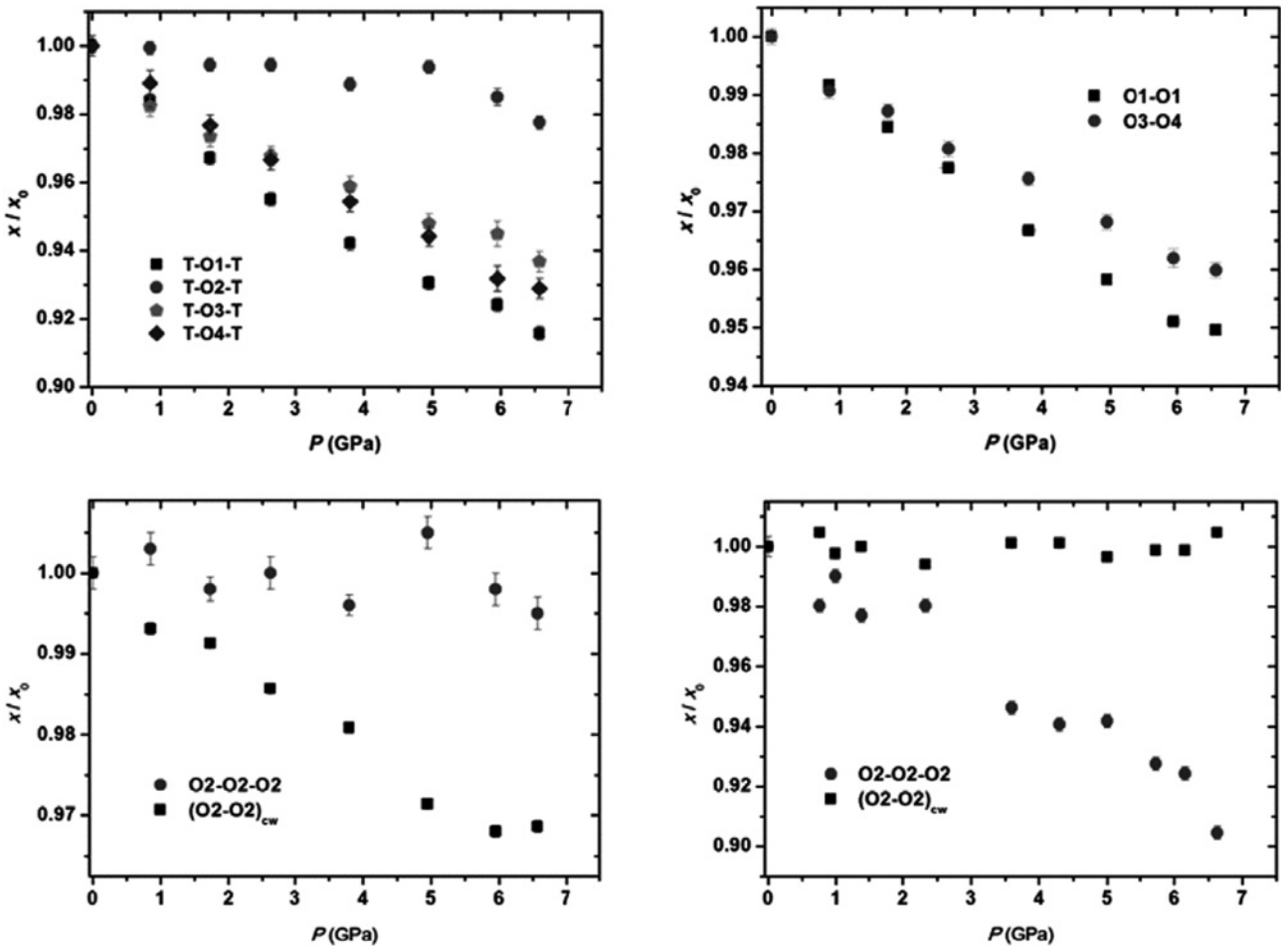

Fig. 7: (*Top*). On the left: *P*-induced evolution of the intertetrahedral Si–O–Al angles, normalized to the room-*P* values. On the right: evolution as a function of pressure of the normalized $(O1–O1)_{ch}$ and $(O3–O4)_{ch}$ channel diameters. (*Bottom*) The *can* unit width $(O2–O2)_{cw}$ and flattening angle (O2–O2–O2), normalized to their values at 0.0001 GPa, as a function of pressure in balliranoite (left) and cancrinite (right). The cancrinite data are from Lotti *et al.* (2012).

dra (Figs. 1, 2), which induces a ditrigonal deformation of the S6R ∠ (0001) windows and a decrease of the hexagonal layer *corrugation* (defined as $\Delta z = (z(O)_{max} - z(O)_{min}) \cdot c$, also originally defined for phyllosilicates by Brigatti and Guggenheim, 2002) (Fig. 2; Table 4).

The contribution of the cage- and channel-voids to the unit-cell volume evolution with pressure has been calculated following the same protocol reported by Lotti *et al.* (2012) for a natural cancrinite. The channel volume has been modeled as $V_{ch} = (\pi R^2) * c$, where $R = [(O1–O1)_{ch} + (O3–O4)_{ch}]/4$, $(O1–O1)_{ch}$ and $(O3–O4)_{ch}$ being the independent channel diameters (Fig. 2). The cage volume has been modeled, by difference, as $V_{cg} = (V_{unit\text{-}cell} - V_{ch})/2$. These volumes, already used by Lotti et al. (2012) and Gatta et al. (2013) for cancrinite-group minerals, do not represent the actual "free voids" of the structure, but they are pure geometric models. Their evolution with pressure has been fitted with a II-BM-EoS, yielding the following refined elastic parameters: $V_{0\,ch} = 326.6(5)$ Å^3 and $K_{0\,Vch} = 36.0(8)$ GPa, $V_{0cg} = 206.7(4)$ Å^3 and $K_{0Vcg} = 66(3)$ GPa, for channel and cage volumes, respectively.

The Ca coordination shell within the *can* unit is a ditrigonal bipyramid (C.N. 8), where the S6R ⊥ [0001] oxygen atoms act as the basis and the neighboring Cl atoms as the apical vertices. A slight decrease with pressure of the three symmetrically related Ca–O2 and of both the independent Ca–Cl bond lengths is observed, whereas no significant deviation from the room-conditions value of the Ca–O1 bond distances occurs (Fig. 4; Table 4). The pressure-induced evolution of the channel cations M–O bond lengths is also reported in Table 4. Both the average $\langle M1–O_f \rangle$ and $\langle M2–O_f \rangle$ bond lengths with framework oxygen atoms, along with the average $\langle M1–O_c \rangle$ bond lengths with carbonate oxygen, undergo a shortening with increasing pressure (Fig. 4; Table 4).

Table 4: Relevant bond distances (Å), voids (Å^3) diameters (Å), angles (°), S6R⊥ [0001] ditrigonal rotation angle α (°), hexagonal layers *corrugation* Δz (Å) and cage/channel-volumes (Å^3) at different pressures.

P (GPa)		0.0001 ($P_{0\text{-DAC}}$)	(P_1) 0.85(3)	(P_2) 1.73(3)	(P_3) 2.62(4)	(P_4) 3.80(5)	(P_5) 4.95(3)	(P_6) 5.95(4)	(P_7) 6.77(2)
Si–	O1	1.602(5)	1.599(6)	1.612(6)	1.624(6)	1.621(5)	1.611(6)	1.609(7)	1.611(6)
	O2	1.598(5)	1.607(5)	1.606(5)	1.591(5)	1.593(5)	1.595(5)	1.582(6)	1.584(6)
	O3	1.635(5)	1.637(5)	1.628(5)	1.618(6)	1.616(5)	1.611(6)	1.612(7)	1.624(6)
	O4	1.618(5)	1.607(5)	1.610(5)	1.619(5)	1.614(5)	1.610(5)	1.609(6)	1.607(5)
	⟨Si–O⟩	1.613	1.613	1.614	1.613	1.611	1.608	1.603	1.607
Al–	O1	1.748(5)	1.743(6)	1.742(6)	1.724(6)	1.713(5)	1.715(6)	1.712(7)	1.716(6)
	O2	1.718(5)	1.698(5)	1.708(5)	1.722(5)	1.717(5)	1.698(5)	1.701(6)	1.705(6)
	O3	1.734(5)	1.745(5)	1.743(5)	1.743(5)	1.736(5)	1.734(5)	1.721(6)	1.713(6)
	O4	1.743(6)	1.745(6)	1.741(5)	1.733(6)	1.740(5)	1.743(6)	1.735(7)	1.751(7)
	⟨Al–O⟩	1.736	1.733	1.734	1.731	1.727	1.723	1.717	1.721
	Si–O1–Al	155.4(3)	152.9(3)	150.3(3)	148.4(3)	146.4(3)	144.6(3)	143.6(3)	142.3(3)
	Si–O2–Al	160.3(3)	160.2(3)	159.4(3)	159.4(3)	158.5(3)	159.3(3)	157.9(4)	156.7(3)
	Si–O3–Al	136.1(4)	133.7(4)	132.5(4)	131.7(4)	130.5(4)	129.0(4)	128.6(5)	127.5(4)
	Si–O4–Al	137.9(4)	136.4(5)	134.7(4)	133.3(4)	131.6(4)	130.2(4)	128.5(5)	128.1(4)
Ca–	O1(x3)	2.614(4)	2.610(5)	2.623(4)	2.624(4)	2.631(5)	2.632(5)	2.626(7)	2.625(6)
	O2(x3)	2.560(4)	2.551(4)	2.544(4)	2.542(4)	2.525(4)	2.536(4)	2.513(5)	2.504(5)
	Cl′	2.650(4)	2.631(3)	2.616(3)	2.596(3)	2.573(3)	2.551(3)	2.526(4)	2.519(4)
	Cl″	2.712(4)	2.705(3)	2.686(3)	2.675(3)	2.657(3)	2.639(3)	2.632(5)	2.638(4)
M1	O1	2.893(5)	2.824(5)	2.744(5)	2.679(5)	2.604(5)	2.555(6)	2.505(8)	2.499(7)
	O3′	2.534(6)	2.481(6)	2.456(6)	2.436(6)	2.399(6)	2.386(7)	2.372(8)	2.356(7)
	O3″	2.584(6)	2.542(7)	2.509(6)	2.478(6)	2.444(6)	2.415(6)	2.379(8)	2.381(7)
	O4′	2.658(6)	2.655(6)	2.671(6)	2.658(6)	2.675(6)	2.654(6)	2.654(8)	2.661(7)
	O4″	2.670(7)	2.688(6)	2.703(6)	2.701(6)	2.720(6)	2.731(7)	2.716(9)	2.727(7)
	O5′	2.507(11)	2.467(11)	2.443(11)	2.440(11)	2.414(11)	2.367(11)	2.368(13)	2.350(12)
	O5″	2.414(9)	2.437(10)	2.453(10)	2.440(10)	2.426(8)	2.405(7)	2.374(10)	2.385(9)
	O5‴	2.462(11)	2.433(11)	2.417(11)	2.395(11)	2.378(10)	2.363(12)	2.348(12)	2.328(12)
	O6′	2.50(2)	2.481(14)	2.452(14)	2.435(14)	2.368(11)	2.323(12)	2.328(14)	2.317(13)
	O6″	2.43(3)	2.40(3)	2.42(3)	2.46(3)	2.61(3)	2.58(3)	2.53(4)	2.52(3)
	O6‴	2.457(14)	2.448(14)	2.426(13)	2.389(13)	2.331(11)	2.319(12)	2.308(14)	2.294(13)
⟨M1–O_{fr}⟩		2.668	2.638	2.617	2.590	2.568	2.548	2.525	2.525
⟨M1–O_{CO3}⟩		2.462	2.444	2.435	2.427	2.421	2.393	2.376	2.366
M2	O1	2.61(2)	2.53(2)	2.49(2)	2.49(2)	2.49(2)	2.40(2)	2.49(3)	2.48(3)
	O3′	2.29(2)	2.23(2)	2.22(2)	2.18(2)	2.14(2)	2.14(2)	2.11(3)	2.10(3)
	O3″	2.26(2)	2.22(2)	2.20(2)	2.18(2)	2.14(2)	2.12(2)	2.10(3)	2.06(3)
	O4′	2.63(2)	2.63(2)	2.64(2)	2.67(2)	2.70(2)	2.67(2)	2.73(3)	2.72(3)
	O4″	2.69(2)	2.70(2)	2.72(2)	2.73(2)	2.77(2)	2.76(2)	2.79(3)	2.83(3)
⟨M2–O_{fr}⟩		2.47	2.45	2.45	2.44	2.44	2.42	2.43	2.43
	M1 ↔ M2	0.77(2)	0.77(2)	0.64(2)	0.59(2)	0.50(2)	0.49(2)	0.42(3)	0.44(3)
	C1–O5	1.297(4)	1.294(4)	1.294(4)	1.298(4)	1.301(5)	1.306(5)	1.300(5)	1.302(5)
	C2–O6	1.301(5)	1.303(5)	1.300(5)	1.296(5)	1.297(5)	1.296(5)	1.296(5)	1.296(5)
	C1 ↔ C2	3.96(6)	3.96(5)	3.87(5)	3.85(5)	4.00(5)	4.06(5)	3.90(6)	3.92(6)
	$(O2–O2)_r$	4.418(7)	4.398(8)	4.379(7)	4.369(8)	4.333(8)	4.345(8)	4.302(10)	4.285(8)
	$(O2–O2)_{cw}$	8.255(5)	8.198(6)	8.183(5)	8.137(5)	8.097(5)	8.019(5)	7.991(6)	7.996(6)
	O2–O2–O2	100.2(2)	100.5(2)	100.0(2)	100.2(2)	99.8(1)	100.7(2)	100.0(2)	99.7(2)
	$(O1–O1)_{ch}$*	9.400(7)	9.323(8)	9.255(8)	9.189(8)	9.087(8)	9.008(8)	8.940(10)	8.927(8)
	$(O3–O4)_{ch}$	8.279(11)	8.202(11)	8.173(10)	8.120(11)	8.077(9)	8.015(11)	7.964(13)	7.947(11)
	φ1 (O1–O4–O3)	138.7(2)	142.2(2)	145.6(2)	147.6(2)	151.3(2)	153.4(2)	155.1(3)	156.4(2)
	φ2 (O1–O3–O4)	138.2(2)	142.0(2)	145.6(2)	147.6(2)	151.3(2)	153.2(2)	154.8(3)	156.1(3)
	φ3 (O4–O3–O1)	100.3(2)	96.9(2)	93.3(2)	91.2(2)	87.7(2)	85.7(2)	84.0(3)	83.0(2)
	φ4 (O3–O4–O1)	100.6(2)	96.8(2)	93.3(2)	91.2(2)	87.6(2)	85.6(2)	84.1(2)	82.8(2)
	S6R⊥ [0001] α	1.2(1)	1.4(1)	1.8(1)	1.9(1)	2.4(1)	2.3(2)	2.7(2)	2.9(2)
	Δz	1.200(9)	1.145(8)	1.093(8)	1.042(8)	0.980(7)	0.942(8)	0.903(10)	0.881(9)
	V_{cg}	326.3(7)	318.6(8)	313.2(7)	307.1(7)	299.5(7)	292.2(7)	286.2(8)	284.8(7)
	V_{ch}	206.4(6)	203.5(7)	202.1(6)	199.8(6)	196.4(5)	193.6(6)	190.5(7)	190.1(6)

* $(O1–O1)_{ch}$ is calculated as the projection onto the (0001) plane of the O1–O1 distance, as the involved O1 atoms are shifted along [0001] of $^1/_2 \cdot z$.

5 Discussion

5.1 Elastic behavior: balliranoite and cancrinite

To the extent of our knowledge, this is the first study on the high-pressure behavior of a davyne subgroup mineral, specifically the (CO_3^{2-})-analogue balliranoite. No evidence of phase transition, structure collapse or change of the compressional behavior has been observed within the pressure range investigated (0.0001–6.77(2) GPa). The refined isothermal bulk modulus at ambient conditions ($K_{V0} = 48(3)$ GPa; $\beta_{V0} = -1/V \cdot (\partial V/\partial P)_{\text{room } T,P} = 1/K_{V0} = 0.021(1)\ \text{GPa}^{-1}$) falls in the range so far reported for open-framework silicates (*i.e.* 18–70 GPa, Gatta 2008) and is comparable to that reported for natural cancrinite (45(2) GPa, Lotti et al. 2012) and synthetic hydroxycancrinite (46(5) GPa, Oh et al. 2011), whereas a slightly lower value was reported for synthetic $Na_6Cs_2Ga_6Ge_6O_{24} \cdot (Ge(OH)_6)$ (36(2) GPa, Gatta and Lee 2008).

Balliranoite shows an anisotropic elastic behavior, with $K_{a0} : K_{c0} = 1.35 : 1$ at ambient pressure. It is worth noting that the [CAN]-framework can be seen as a "layered structure", as described in Section 1, and the most compressible direction is that perpendicular to the stacking plane of the hexagonal layers.

Cancrinite showed an apparent subtle change of the compressional behavior at $4.62(2) \leq P\ (\text{GPa}) \leq 5.00(2)$, as reported by Lotti et al. (2012), with refined elastic parameters $K_{V0} = 45(2)$ GPa and $K'_V = 6(1)$ (within 0.0001–4.62 GPa), $K_{V0} = 40(2)$ GPa and $K'_V = 4$ (fixed) (within 5.00–6.62 GPa). Besides the refined isothermal bulk moduli, the balliranoite and cancrinite normalized unit-cell volumes (i.e. $V/V_{\text{room-}P}$) evolution with pressure, shown in Fig. 8, suggests that these isotypic minerals share a similar volume compressibility. However, as shown by the pressure-induced evolution of the normalized *a* and *c* unit-cell parameters ($l/l_{\text{room-}P}$) (Fig. 8), balliranoite is characterized by a less pronounced anisotropic pattern: i.e., compared to cancrinite, it presents a higher compressibility within the (0001) plane and a higher stiffness along the most compressible direction [0001]. These combined features lead to the aforementioned similar volume compressibility.

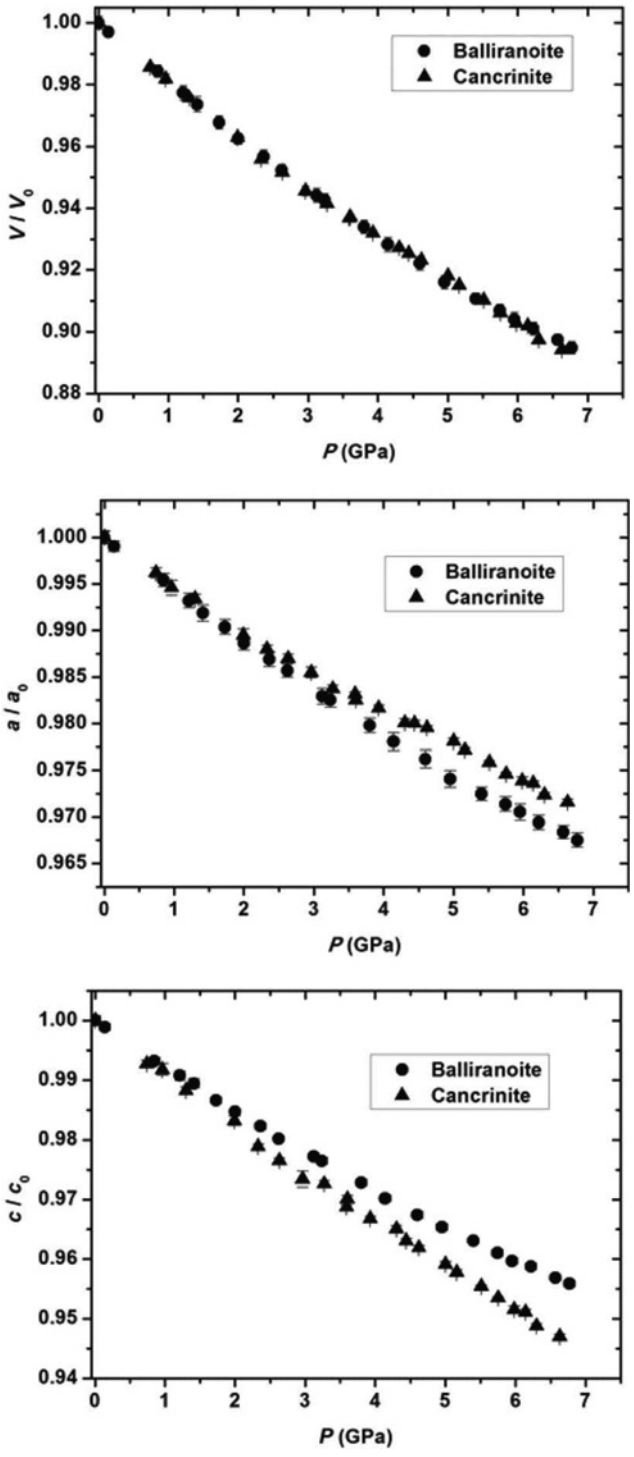

Fig. 8: *P*-induced evolution of the normalized unit-cell volume, *a* and *c* parameters, respectively, in balliranoite (circles) and cancrinite (triangles). Cancrinite data are from Lotti *et al.* (2012).

5.2 High-pressure structure evolution

Although a slight compression of the AlO_4 tetrahedra can be inferred from the average ⟨Al–O⟩ bond lengths (Table 4), the *P*-induced structure evolution of balliranoite is mainly driven by the tilting of the perfectly ordered framework, as shown by the Si–O–Al intertetrahedral angles (Fig. 7; Table 4).

The shrinking of the unit-cell volume is accommodated along the softest [0001] crystallographic direction

by the compression of the double chain of tetrahedra (*dzc* unit) (Figs. 1, 2, Table 4), whereas within the (0001) plane can be described as accommodated by the combination of two concomitant mechanisms: 1) the *can* unit compression, through the $(O2–O2)_{cw}$ shortening (Figs. 2, 7; Table 4) and 2) the S6R ⊥ [0001] ditrigonal rotation, through the $(O2–O2)_R$ contraction (Fig. 2; Table 4). The refined elastic behavior of the cage- and channel-volumes shows that the bulk volume compression is mainly achieved through the channel voids, since it is $K_{0Vch} : K_{0Vcg} = 1 : 1.83$.

If we assume a full occupancy of the Ca and Cl sites within the *can* units, as suggested by the structure refinements, the chemical analysis of our balliranoite (reported by Gatta et al. 2013) indicates that the crystal chemistry of the channel population can be expressed as $Na_{4.47}Ca_{0.86}K_{0.11}(CO_3)_{0.78}(SO_4)_{0.33}$, which corresponds to 68.46 and 40.33 e^-/unit-cell, for cationic and anionic population, respectively. The structure refinement, based on the data collected with the crystal in air, has been performed using the neutral scattering factor of Na for both the M1 and M2 sites, yielding the following site occupancy factors: 0.881(6) and 0.160(6), respectively. These values correspond to $((0.881+0.160) \cdot 6) \cdot 11 = 68.71$ e^-/unit-cell, in excellent agreement with the chemical data. Assuming that all Ca and K occupy the M1 site, because of more favorable bond lengths (Table 4), the following composition is derived for M1: 59% Na, 14% Ca and 2% K with 25% of vacancies, whereas M2 is 16% occupied by Na. The refined electrons content from the modeled anionic groups (C1–O5 and C2–O6) is given by $((0.56 + 0.22) \cdot 2) \cdot 6 + ((0.575 + 0.165) \cdot 6) \cdot 8 = 44.88$ e^-/unit-cell. The slight discrepancy between the refined anionic content and that expected from the chemical analysis is not surprising if we consider the highly disordered distribution of the electron density along the 6_3 axis, as shown by the difference-Fourier maps (Fig. 5). A comparable disorder was also reported by Della Ventura et al. (2007) for a natural sample of vishnevite, the SO_4^{2-} end-member of the cancrinite subgroup, along with a similar discrepancy between structure refinement and chemical analysis for the anionic groups. The refined anisotropic displacement parameters of the carbonate groups sites show unrealistically high U_{33} values (Fig. 4; deposited Table). This feature was already reported for cancrinite (Balliranno and Maras 2004; Della Ventura et al. 2009; Gatta et al. 2012) and Gatta et al. (2013) showed that, in balliranoite, it is preserved at low-temperature at least down to 108 K. As proposed by several authors for cancrinite (e.g. Grundy and Hassan 1982; Gatta et al. 2012) and discussed by Gatta et al. (2013) for balliranoite, the strong anisotropy exhibited by the displacement parameters of the (CO_3^{2-})-groups, along with the aplanarity between the average positions of the carbon and related oxygen atoms (Table 3), is a further hint of their positional disorder along the *c*-axis. The disorder of the extra-framework population hinders a realistic refinement of the site occupancy factors and, thus, of the total electron content of the anionic groups.

The M1 and M2 cationic sites have the same configuration reported by Gatta et al. (2013) and Chukanov et al. (2010). M1 lies closer to the channel center and is likely too far from O1 for an effective bond when it is occupied by Na. As a consequence, it is coordinated by 4 framework oxygen atoms on one side (5 with O1) and up to 3 carbonate oxygen atoms on the other side. However, the statistical distribution, the occurrence of vacancies and the positional disorder of the anionic population result in a non-univocal coordination environment. Conversely, the M2 site is closer to the channel walls and is coordinated by 5 framework oxygen atoms, whereas, according to the bond valence method (Brown 2002), the M2–(O5, O6) distances are too long for effective bonds. The loss of the contribution given to the total bond valence by the M–(O5,O6) bonds would be partially compensated by the shorter $M2–O_f$ distances with framework oxygen atoms, suggesting the occurrence of M2 likely coupled with vacancies within the neighboring anionic sites. An inspection of the pressure-induced evolution of the M–O bond lengths (Table 4) shows that with increasing pressure: 1) O1 progressively falls within the Na(M1) coordination shell and 2) O5–O6 are more bound to M2. Furthermore, the distance between the M1 and M2 average positions continuously decreases (Fig. 3; Table 4). In this light, test refinements have been performed in order to investigate a potential merging of the M sites. Although the full merging in a single site cannot be unambiguously proved, the decrease of the M1 ↔ M2 distance and the very similar coordination environment shown by the M1 and M2 cations at the higher pressures suggest this tendency.

The configuration of the *can* units population is simpler than the channel one: three upwards and three downwards mutually exclusive Ca–Cl bonds can occur, due to the Cl positioning out of the 3-fold axis, but the ditrigonal bipyramid coordination is always preserved (Fig. 4). The *P*-induced evolution of the Ca–O and Ca–Cl bonds (Table 4) shows a slight re-arrangement related to the S6R ⊥ [0001] ditrigonalization and a compression of the Ca–Cl chains which follows that of the *dzc* units.

It is worth noting that, though with a significantly lower magnitude and, hence, without the effects pertain-

ing to the channel cations coordination shells, the same deformation mechanisms have also been described for the low temperature ($108 \leq T$ (K) ≤ 293) structure evolution of the same natural balliranoite (Gatta et al. 2013). A similar analogy between the effects induced by these "compressive" regimes (low-T and high-P), was already reported for the isotypic cancrinite (Gatta et al. 2012; Lotti et al. 2012).

5.3 Comparison with the cancrinite behavior at high pressure

The occurrence of Ca–Cl chains within the *can* units of balliranoite, in place of the Na–H_2O chains occurring in cancrinite, gives rise to an expansion of the [CAN]-framework, as shown by the higher unit-cell volume and by the higher values of all the Si–O–Al intertetrahedral angles in balliranoite at room conditions (Lotti et al. 2012). The influence of the extraframework population is not only limited to the structure configuration at ambient conditions, but apparently plays a role also on the high-pressure structure evolution. In cancrinite, in fact, all the intertetrahedral angles decrease with pressure, whereas in balliranoite only a slight deviation from the room-P value of the Si–O2–Al is shown (Fig. 7; Table 4). The resulting different tetrahedral tilting shows the largest effects within the (0001) plane. Compared to cancrinite, the S6R $\perp$ [0001] ditrigonal rotation angle in balliranoite is smaller at ambient conditions ($\alpha_{BAL} = 1.2(1)°$, $\alpha_{CAN} = 8.8(2)°$) and its increase with pressure is significantly less intense. This is correlated to the different P-induced behavior shown by the cations-framework oxygen bonds of the cage population. In cancrinite, a strong compression of the shorter Na–O2 and a stretching of the longer Na–O1 bonds are observed at high pressure (Lotti et al. 2012). In balliranoite, a less pronounced shortening of the Ca–O2 bonds occurs, whereas no significant changes of the Ca–O1 distances is observed (Fig. 4; Table 4).

A considerably different deformation of the *can* unit can also be described between these isotypic compounds. In balliranoite, the shortening along the $(O2–O2)_{cw}$ ("cage width") is coupled with a same magnitude compression of the *dzc* unit along [0001]. As a consequence no significant change of the cage flattening angle O2–O2–O2 (Figs. 2, 7; Table 4) is observed, so that the cage undergoes a homogeneous shrinking. In cancrinite, the *can* unit behavior is opposite: the compression of the double chain of tetrahedra is not counterbalanced by a shortening along $(O2–O2)_{cw}$ and the closure of O2–O2–O2 reflects the "flattening" of the *can* unit with pressure (Lotti et al. 2012). Significant differences are also observed in the channel deformation. In our balliranoite, both the independent diameters are compressed with increasing pressure (Figs. 2, 7; Table 4), leading to a continuous shortening of the channel "free diameter" along O3–O4 (Baerlocher et al. 2007): from 5.58(1) Å at room-P to 5.25(1) Å at 6.77(2) GPa). Conversely, in cancrinite, only the O1–O1 diameter undergoes a significant shortening, keeping almost constant the channel "free diameter" at the lower pressures, since, along the O3–O4 direction, compression is mainly accommodated by the S4R deformation (Lotti et al. 2012). Furthermore, the different *can* units population leads to a stretching of the S4R along O3–O4 at ambient conditions in balliranoite, which is partially counterbalanced with a shorter $(O3–O4)_{ch}$ (i.e. a shorter channel free diameter, 5.58(1) Å in balliranoite, 5.78(1) Å in cancrinite).

Besides the large differences observed within the (0001) plane, the same deformation mechanism is shown along [0001], i.e. the compression of the double chain of tetrahedra (*dzc* unit), even though with a different magnitude.

6 Conclusions

This study on a natural balliranoite from Mogok (Myanmar) represents, to the best of our knowledge, the first investigation on the high-pressure behavior of a davyne subgroup mineral. The studied sample is stable up to the highest pressure here investigated (6.77(2) GPa) and the refined elastic parameters are comparable with those of other cancrinite-group minerals (Lotti et al. 2012; Oh et al. 2011). The P-induced structure evolution is mainly governed by the tilting of framework tetrahedra, acting as quasi-rigid units. This tilting is reflected within the (0001) plane by the ditrigonal rotation of the S6R $\perp$ [0001] and by the cage compression through the $(O2–O2)_{cw}$ shortening, and along [0001] by the compression of the double chain of tetrahedra (*dzc* unit). An apparent re-arrangement of the channel cationic population occurs, described by the tendency of the two M sites to merge.

The comparison with the isotypic cancrinite (Lotti et al. 2012) shows a similar volume compressibility, but a less pronounced elastic anisotropy. The observed different elastic behavior is due to different deformation mechanisms. The largest differences are observed within the (0001) plane, where different evolution of *can* units and channels occur.

The results obtained in this study and those of the low-T investigation of natural balliranoite (Gatta et al. 2013) suggest that the nature of the extraframework po-

pulation of the *can* units has a considerable influence on the structure deformation mechanisms at non-ambient conditions and, hence, on the thermo-elastic behavior of the cancrinite-group minerals. Further studies on vishnevite and davyne are in progress.

Acknowledgements: This work was funded by the Italian Ministry of Education, MIUR-Project: "Futuro in Ricerca 2012 – ImPACT-RBFR12CLQD". Two anonymous reviewers and the Guest Editor R. J. Angel are thanked

References

Agilent, *Xcalibur CCD system, Crysalis software system*, Abingdon **2012**.

R. J. Angel, Equations of state. In: *High-Temperature and High-Pressure Crystal Chemistry* (Eds. R. M. Hazen, R. T. Downs) Reviews in Mineralogy and Geochemistry, Vol. 41, pp. 35–60. Mineralogical Society of America and Geochemical Society (Washington DC, USA) 2000.

R. J. Angel, *J. Appl. Crystallogr.* **2004**, *37*, 486–492.

R. J. Angel, D. R. Allan, R. Miletich, L. W. Finger, *J. Appl. Crystallogr.* **1997**, *30*, 461–466.

R. J. Angel, M. Bujak, J. Zhao, G. D. Gatta, S. Jacobsen, *J. Appl. Crystallogr.* **2007**, *40*, 26–32.

C. Baerlocher, L. B. McCusker, D. H. Olson, *Atlas of zeolite framework types*, 6th ed. Elsevier, Amsterdam **2007**.

P. Ballirano, A. Maras, *Eur. J. Mineral.* **2004**, *16*, 135–141.

P. Ballirano, A. Maras, P. R. Buseck, *Am. Mineral.* **1996**, *81*, 1003–1012.

P. Ballirano, E. Bonaccorsi, S. Merlino, A. Maras, *Can. Mineral.* **1998**, *36*, 1285–1292.

R. M. Barrer, J. D. Falconer, *Proc. Royal Soc.* **1956**, *236*, 227–249.

J. Binon, E. Bonaccorsi, H. J. Bernhardt, A. M. Fransolet, *Eur. J. Mineral.* **2004**, *16*, 511–520.

F. Birch, *Phys. Rev.* **1947**, *71*, 809–824.

E. Bonaccorsi, S. Merlino, Modular Microporous Minerals: Cancrinite-Davyne Group and C-S-H Phases. In: *Micro- and Mesoporous Mineral Phases* (Eds. G. Ferraris, S. Merlino), Reviews in Mineralogy and Geochemistry, Vol. 57, pp. 241–290. Mineralogical Society of America and Geochemical Society (Washington DC, USA) 2005.

E. Bonaccorsi, S. Merlino, M. Pasero, *N. Jb. Mineral.Mh.* **1990**, 97–112.

E. Bonaccorsi, S. Merlino, P. Orlandi, M. Pasero, G. Vezzalini, *Eur. J. Mineral.* **1994**, *6*, 481–487.

E. Bonaccorsi, P. Comodi, S. Merlino, *Phys. Chem. Mineral.* **1995**, *22*, 367–374.

E. Bonaccorsi, S. Merlino, M. Pasero, G. Macedonio, *Phys. Chem. Mineral.* **2001**, *28*, 509–522.

E. Bonaccorsi, G. Della Ventura, F. Bellatreccia, S. Merlino, *Micropor. Mesopor. Mater.* **2007**, *99*, 225–235.

M. F. Brigatti, S. Guggenheim, Mica crystal chemistry and the influence of pressure, temperature, and solid solution on atomistic models. In: *Micas: Crystal Chemistry and Metamorphic Petrology* (Eds. A. Mottana, F. P. Sassi, J. B. Thompson, S. Guggenheim), Reviews in Mineralogy and Geochemistry, Vol. 46, pp. 1–98. Mineralogical Society of America and Geochemical Society (Washington DC, USA) 2002.

I. D. Brown, *The Chemical Bond in Inorganic Chemistry. The Bond Valence Method.* Oxford University Press, Oxford **2002**.

N. V. Chukanov, N. V. Zubkova, I. V. Pekov, L. V. Olysych, E. Bonaccorsi, D. Y. Pushcharovsky, *Eur. J. Mineral.* **2010**, *22*, 113–119.

W. A. Deer, R. S. Howie, W. S. Wise, J. Zussman, *Rock-forming minerals. Framework silicates: silica minerals, feldspathoids and the zeolites*, Vol. 4B, The Geological Society, London **2004**.

G. Della Ventura, F. Bellatreccia, G. C. Parodi, F. Cámara, M. Piccinini, *Am. Mineral.* **2007**, *92*, 713–721.

G. Della Ventura, G. D. Gatta, G. J. Redhammer, F. Bellatreccia, A. Loose, G. C. Parodi, *Phys. Chem. Mineral.* **2009**, *36*, 193–206.

L. J. Farrugia, *J. Appl. Crystallogr.* **1999**, *32*, 837–838.

M. Fechtelkord, F. Stief, J. C. Buhl, *Am. Mineral.* **2001**, *86*, 165–175.

G. D. Gatta, *Z. Kristallogr.* **2008**, *223*, 160–170.

G. D. Gatta, Y. Lee, *Micropor. Mesopor. Mater.* **2008**, *116*, 51–58.

G. D. Gatta, P. Lotti, V. Kahlenberg, U. Haefeker, *Mineral. Mag.* **2012**, *76*, 933–948.

G. D. Gatta, P. Lotti, V. Kahlenberg, *Micropor. Mesopor. Mater.* **2013**, *174*, 44–53.

H. D. Grundy, I. Hassan, *Can. Mineral.* **1982**, *20*, 239–251.

G. E. Harlow, W. Bender, *Am. Mineral.* **2013**, *98*, 1120–1132.

I. Hassan, *Can. Mineral.* **1996**, *34*, 893–900.

I. Hassan, H. D. Grundy, *Can. Mineral.* **1990**, *28*, 341–349.

I. Hassan, S. Antao, J. B. Parise, *Am. Mineral.* **2006**, *91*, 1117–1124.

D. L. Heinz, R. Jeanloz, *J. Appl. Phys.* **1984**, *50*, 885–893.

P. Lotti, G. D. Gatta, N. Rotiroti, F. Cámara, *Am. Mineral.* **2012**, *97*, 872–882.

L. B. McCusker, F. Liebau, G. Engelhardt, *Pure Appl. Chem.* **2001**, *73*, 381–394.

R. Miletich, D. R. Allan, W. F. Kuhs, High-Pressure Single-Crystal Techniques. In: *High-Temperature and High-Pressure Crystal Chemistry* (Eds. R. M. Hazen, R. T. Downs), Reviews in Mineralogy and Geochemistry, Vol. 41, pp. 445–520. Mineralogical Society of America and Geochemical Society (Washington DC, USA) 2000.

J. E. Oh, S. M. Clark, P. J. Monteiro, *Cement Concrete Comp.* **2011**, *33*, 1014–1019.

I. V. Pekov, L. V. Olysych, N. V. Chukanov, N. V. Zubkova, D. Y. Pushcharovsky, *Can. Mineral.* **2011**, *49*, 1129–1150.

K. A. Rozenberg, R. K. Rastsvetaeva, N. V. Chukanov, C*rystallogr. Rep.* **2009**, *54*, 793–799.

G. M. Sheldrick, *Acta Cryst.* **2008**, *A64*, 112–122.

M. Sirbescu, D. M. Jenkins, *Am. Mineral.* **1999**, *84*, 1850–1860.

A. J. C. Wilson, E. Prince, *International Tables for Crystallography volume C, Mathematical, Physical and Chemical Tables*, 2nd ed., Kluwer, Dordrecht **1999**.

Received March 18, 2013; accepted May 21, 2013
Published online November 15, 2013